

Supporting Information for

**d¹⁰ or d⁰? Theoretical and experimental comparison
between rutile GeO₂ and TiO₂ for photocatalytic water
splitting**

Table of Contents

1. Syntheses and characterizations
2. Experimental details for photocatalytic water splitting
3. Theoretical calculations
4. Crystal structure and phonon dispersion spectra of rutile GeO_2 and TiO_2
5. COHP figures of corresponding orbital pair interactions to rutile GeO_2 and TiO_2
6. Molecular orbital schemes for TiO_6 and GeO_6 octahedron
7. The first Brillouin zone of rutile structure
8. Orbital-solved band structure/ partial density of state for rutile SnO_2
9. Crystal structure and orbital-solved band structure/ partial density of state for α -quartz GeO_2
10. Le Bail fitting to the PXRD of rutile GeO_2
11. SEM and TEM images for rutile GeO_2
12. Raman spectrum of rutile GeO_2
13. XPS spectrum of rutile GeO_2
14. UV-Vis diffuse reflectance spectra of rutile GeO_2
15. Photocatalytic H_2 evolution rate for rutile TiO_2 , GeO_2 , and GeO_2 loaded various cocatalysts
16. Repeating photocatalytic experiment for rutile GeO_2 in pure water
17. Powder XRD for rutile GeO_2 before and after the photocatalytic reactions
18. Powder XRD for rutile GeO_2 and the melon- GeO_2 composite
19. High-resolution XPS spectra of the melon- GeO_2 composite
20. UV Raman spectra of the melon- GeO_2 composite
21. Typical thermogravimetric curve of the melon- GeO_2 composite
22. UV-vis spectra of the melon- GeO_2 composite
23. Repeating photocatalytic experiments for the melon- GeO_2 composite
24. Work functions for monolayer melon, GeO_2 (100) surface, and the melon- GeO_2 composite
25. The band alignment of GeO_2 and melon before contacting

26. Table of calculated effective mass of charges for rutile TiO_2 and GeO_2
27. Table of calculated effective masses of charges for rutile SnO_2
28. Table of calculated effective mass of charges for α -quartz GeO_2
29. The calculation of the potentials of CB and VB edges for rutile GeO_2
30. References

1. Syntheses and characterizations

1.1 Syntheses

Rutile GeO₂ was synthesized via a hydrothermal method. To be specific, 2.5 mmol of commercial GeO₂ (99.99%) and 5 mL of concentrated HNO₃ aqueous solution were placed in a 25 mL Teflon-lined stainless-steel autoclave and heated at 240 °C for 2 days. After cooling, the resultant white powder was washed extensively with deionized water and dried at 80 °C.

To obtain the melon-modified rutile GeO₂, a mixture of 0.2 g rutile GeO₂ and 1.0 g urea was ground for 30 min in an agate mortar. This mixture was calcined at 400 °C for 1 h. The resultant yellow powder was washed thereafter with diluted HNO₃, ethyl alcohol and distilled water to remove any residual soluble component. The final powder was dried at 80 °C for further characterizations.

1.2 Characterizations

The phase purity and crystallinity of the powder samples were characterized by laboratory powder X-ray diffraction (PXRD) on a PANalytical Empyrean diffractometer (Cu K α radiation). The operation voltage and current were 40 kV and 40 mA, respectively. Le Bail refinement was performed using the TOPAS software.¹ Scanning and transmission electron microscopy (SEM and TEM) were performed on JSM-7800F and JEM-2100 electron microscopes, respectively. The UV-vis diffused reflectance spectra (DRS) were recorded at room temperature using a UV-visible-near infrared spectrometer (Shimadzu UV-3600) equipped with an integrating sphere attachment. BaSO₄ was used as reflectance standard. Laser Raman spectra were recorded on a LabRAM HR Evolution and at a spectral resolution of 2 cm⁻¹. X-ray photoelectron spectra (XPS) was acquired with an Escalab 250xi photoelectron spectrometer with Ag K α X-ray source. Thermogravimetric (TG) analyses for the melon-GeO₂ composite was performed on a Shimadzu DTG-60H instrument at a heating rate of 10 °C /min from room temperature to 900 °C under air condition.

2. Experimental details for photocatalytic water splitting

Photocatalytic hydrogen evolution was tested on a gas-closed circulation system equipped with a vacuum line (CEL-SPH2N system), a 150 mL Pyrex glass reactor with a quartz cover, and a gas sampling port that is directly connected to a gas chromatograph (Shanghai Techcomp-GC7900, TCD detector, molecular sieve 5A, N₂ gas carrier). In a typical run, 50 mg of catalyst was dispersed by a magnetic stirring bar in 50 mL of pure water or 20 vol.% methanol aqueous solution. A 10 °C recycling water bath was applied to keep the reaction vessel at a constant temperature. Pt, Ni, Ru, Pd, Ag, Au was loaded onto sample powders through photo-deposition method according to literature.²

3. Theoretical calculations

All calculation results were obtained by first-principles calculation, implemented in Vienna Ab-initio Simulation Package (VASP).³ The projector augmented-wave (PAW) method implemented in the VASP code was utilized to describe the interaction between the ionic cores and the valence electrons.⁴ The generalized gradient approximation (GGA) parameterized by Perdew, Burke, and Ernzerhof (PBE) was employed to describe the exchange-correlation potential in the standard Density Function Theory (DFT) calculations.⁵ An energy cutoff of 600 eV and 4×4×6 k-point with a G centered k mesh were used for structure optimization. To correct the underestimated band gap value, the HSE06 hybrid functional was utilized to evaluate the electronic properties.⁶ For the default HSE06 functional, the 1/4 of PBE exchange is replaced by the Hartree-Fock exact exchange. Namely, the Hartree-Fock exchange mixing parameter (α) in the HSE06 functional is set to be 0.25. The carrier effective mass is evaluated from the second derivative of the highest point of the VB and the

lowest point of the CB according to $E = \frac{\hbar^2 k^2}{2m_e m^*}$, where m_e denotes the free electron mass (9.1×10^{-31} kg).

The carrier mobility was calculated using the following formula:⁷

$$\mu = \frac{(8 \times \pi)^{1/2} \times e \times \hbar^4 \times \rho \times v^2}{3 \times (m^*)^2 \times E_d^2 \times (\kappa_B T)^2}$$

In this approach, the primary carrier scattering mechanism is dominated by the acoustic phonon scattering. The e , \hbar , ρ , v , m^* , E_d , κ_B , T are the elementary charge, the reduced Planck constant, the density, the longitudinal sound velocity, the effective mass, the DP (deformation potential) constant, the Boltzmann constant, and temperature, respectively. The DP constant was computed by $E_d = \frac{\partial E}{\partial l/l_0}$ (where l_0 is the equilibrium lattice parameter). E_d for electrons and holes are calculated based on the energy change of the VBM and CBM, respectively. The corresponding lattice parameter changes are $0.99l_0$, $0.995l_0$, l_0 , $1.005l_0$, $1.01l_0$. The longitudinal sound velocity can be obtained from the phonon band dispersion along the different directions, the value is the slope of the acoustic phonon dispersion around the Γ site.

For chemical bonding analyses, we utilized the COHP method as calculated by the LOBSTER package,⁸ which reconstructs the orbital-resolved electronic structure via projection of the PAW wave functions onto atomic-like basis functions.

The work functions (WFs) were obtained by calculating the electrostatic potential in the vacuum (c) axis, and WF is defined as $E_{\text{vacuum}} - E_{\text{fermi}}$. A monolayer melon ($\text{H}_{12}\text{C}_{24}\text{N}_{36}$) was constructed to represent the incomplete polycondensation.⁹ In the present study, due to the crystal growth directions limited by the tetragonal symmetry of GeO_2 , a GeO_2 (100) surface (3×6) was used to match with the monolayer melon lattice ($a = 12.58 \text{ \AA}$, $b = 17.01 \text{ \AA}$), and the lattice mismatch was less than 10%. To save the calculated cost, we adopt 3-layer (162 atoms) structures for GeO_2 (100) surface. A 15 \AA vacuum region was used to prevent the interaction between top and bottom atoms in all surface systems. In addition, the dipole correction and the effect of van der Waals interactions were considered in GeO_2 (100) surface and the interfacial structure.

4. Crystal structure and phonon dispersion spectra of rutile GeO_2 and TiO_2

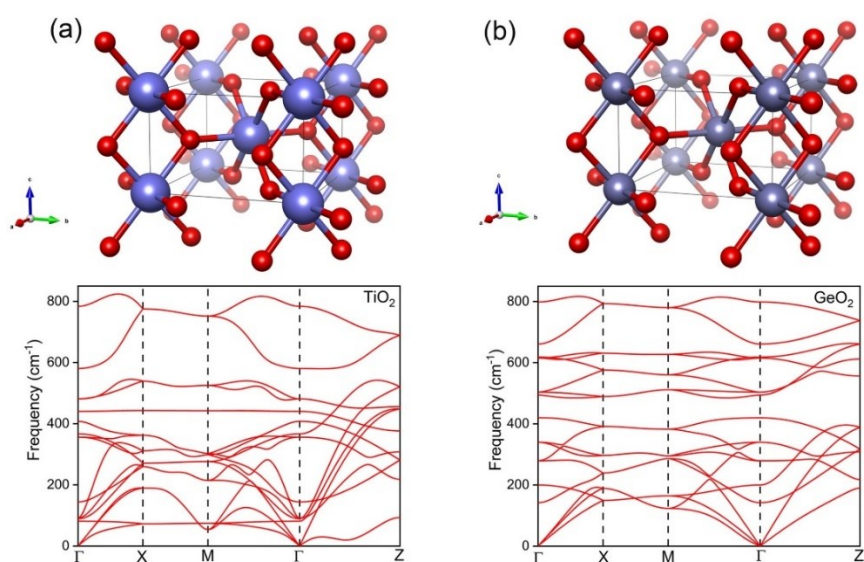


Figure S1. The crystal structure and phonon dispersion spectra of rutile (a) TiO_2 and (b) GeO_2 . Blue, gray, red spheres represent Ti, Ge, and O atoms, respectively.

5. COHP figures of corresponding orbital pair interactions to GeO_2 and TiO_2

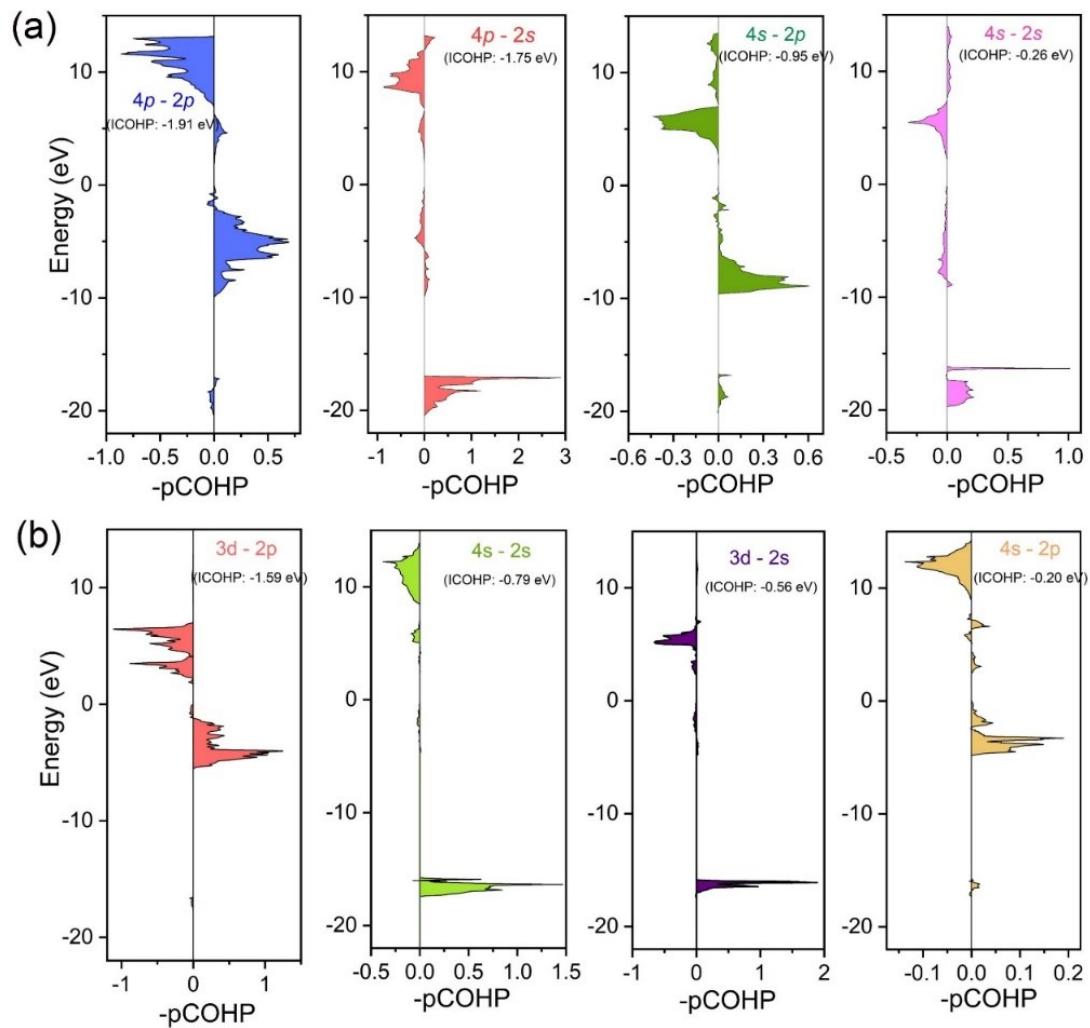


Figure S2. The ICOHP values (in eV/bond) of the corresponding orbital pair contributions to (a) GeO_2 and (b) TiO_2 .

6. Molecular orbital schemes for TiO_6 and GeO_6 octahedron

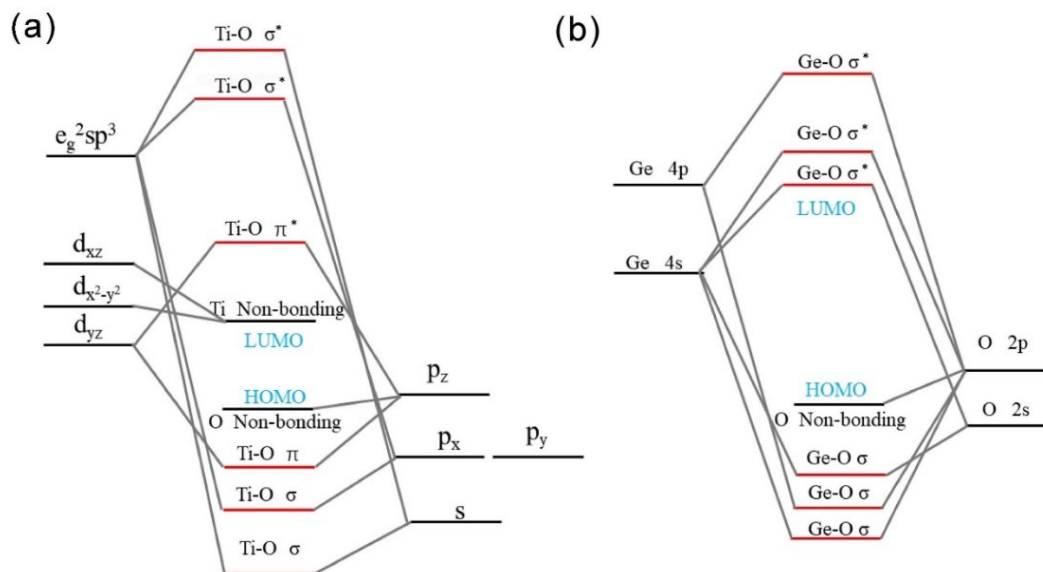


Figure S3. Molecular-orbital scheme for MO_6 octahedron ($M = \text{Ti}$ and Ge).

The coordinate system is defined as: $x//[001]$, $y//[110]$, $z//[10]$. For TiO_6 with d^0 electron configuration, outer Ti 3d orbitals will split into e_g and t_{2g} orbitals (In fact, the symmetry of TiO_6 octahedron is D_{2h} due to the different Ti-O bond lengths for in-plane (equatorial) and out-of-plane (axial), which deviate from the ideal O_h symmetry. For convenience, we still adopt the well-known symmetry classification of t_{2g}/e_g on labelling). And then, in order to adapt the octahedral geometry, two e_g orbitals combining Ti 4s and 4p orbitals to form six hybridized orbitals bonding with six adjacent O atoms. Notably, the partial of t_{2g} orbitals will form non-bonding orbitals, which makes up LUMO for molecular orbitals.¹⁰ Meanwhile, the other t_{2g} orbitals bond with O $2p_z$ orbitals in result of compatible symmetries and similar energies. Another important point is that an oxygen atom is surround by three Ti atoms and the Ti_3O units exhibited a ‘Y’ geometric configuration. Thus, the sp^2 hybridization will occur and another p orbital form non-bonding orbital, which constitutes HOMO for molecular orbitals. By contrast, owing to the screening for d orbitals on GeO_6 , outer s and p orbitals tend to bond with O atoms.¹¹ A partial of O-p orbitals will form HOMO and the LUMO will composed of Ge-O σ -type anti-bonding orbital.

7. The first Brillouin zone of rutile structure

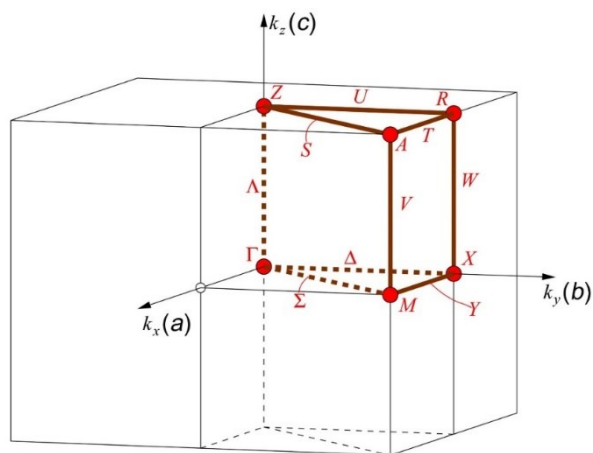


Figure S4. The first Brillouin zones of the rutile structure with high-symmetry points.

8. Orbital-solved band structure/ partial density of state for rutile SnO₂

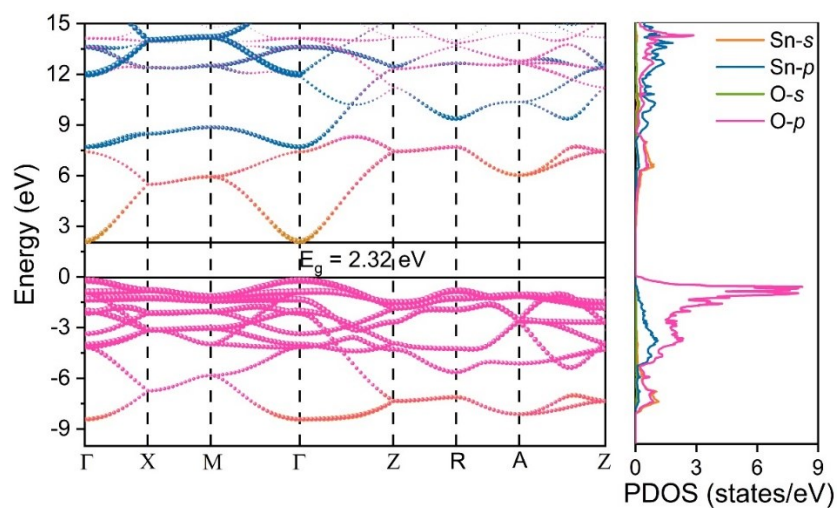


Figure S5. The band structure and partial density of state for rutile SnO₂.

9. Crystal structure and orbital-solved band structure/ partial density of state for α -quartz GeO_2

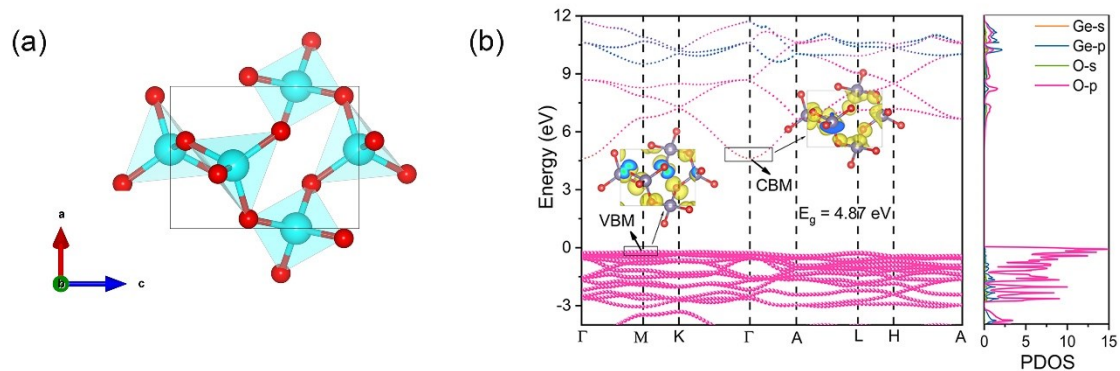


Figure S6. (a) crystal structures for α -quartz GeO_2 along b axis, the sky blue and red balls denote Ge atoms and O atoms, respectively; (b) Orbital-resolved band structure and density of state for α -quartz GeO_2 . The inset is the spatial distribution of partial charge densities of the VBM and CBM states for α -quartz GeO_2 with an iso-value of 0.005 electron/bohr³.

10. Le Bail fitting to the PXRD of rutile GeO_2

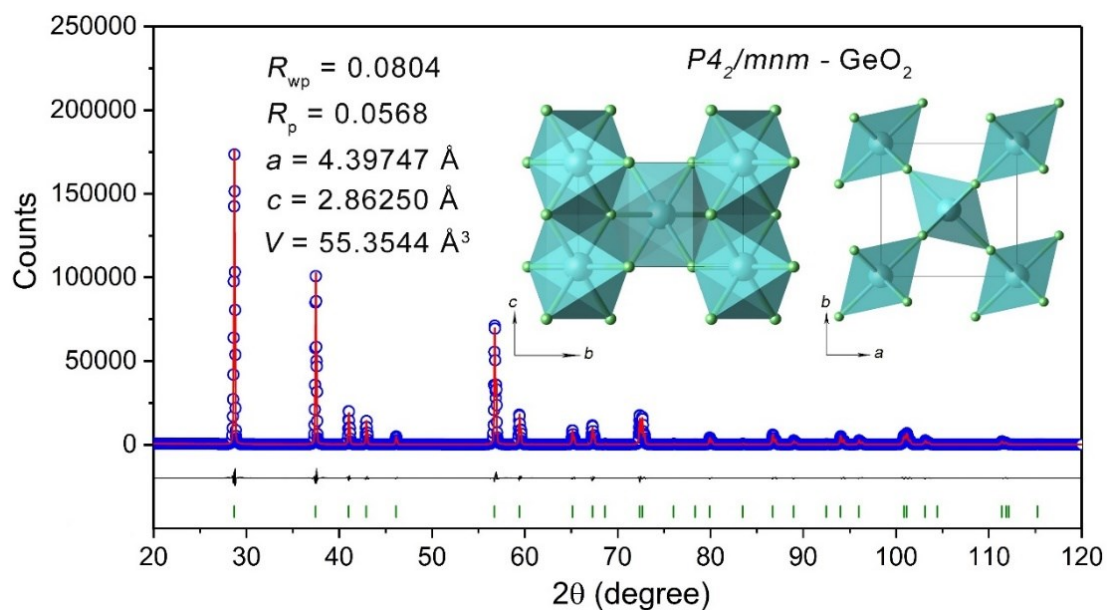


Figure S7. Le Bail fitting to the PXRD of rutile GeO_2 . The blue cycles and red line represent the observed and calculated data, respectively. Cell parameters and agreement

factor are also listed. The right insert shows the views of crystal structures for rutile GeO_2 along the a and c axes, respectively.

11. SEM and TEM images for rutile GeO_2

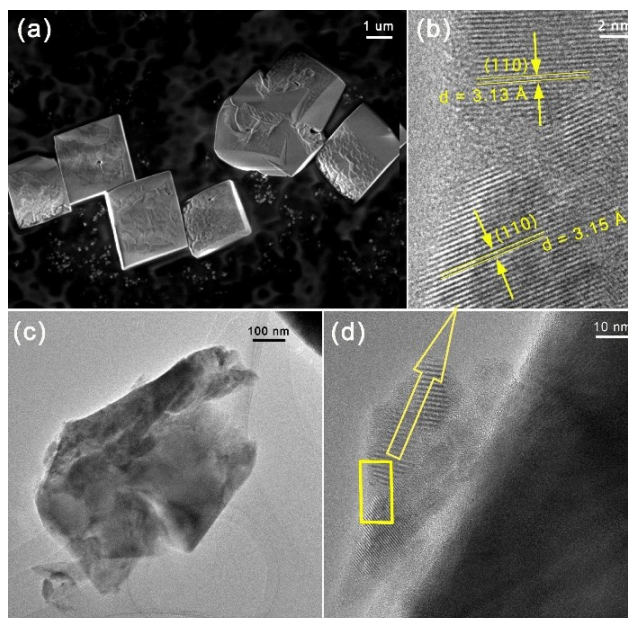


Figure S8. (a) SEM image for as-prepared rutile GeO_2 . (b) shows the high resolution image of rutile GeO_2 . (c) and (d) represent the TEM images of rutile GeO_2 .

12. Raman spectrum of rutile GeO_2

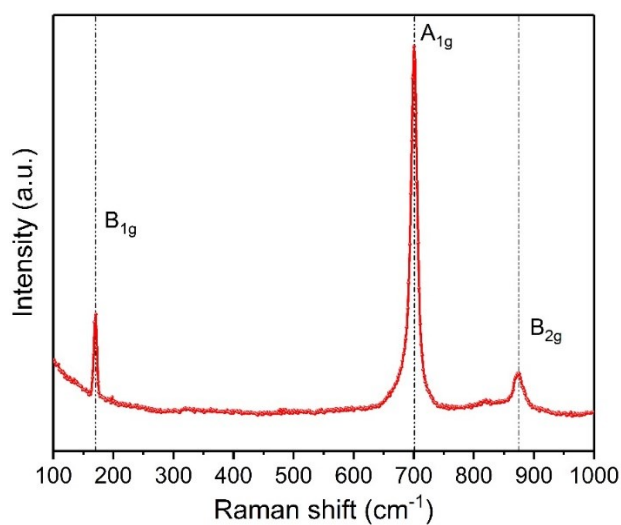


Figure S9. Raman spectrum of the rutile-type GeO_2 .

13. XPS spectrum of rutile GeO₂

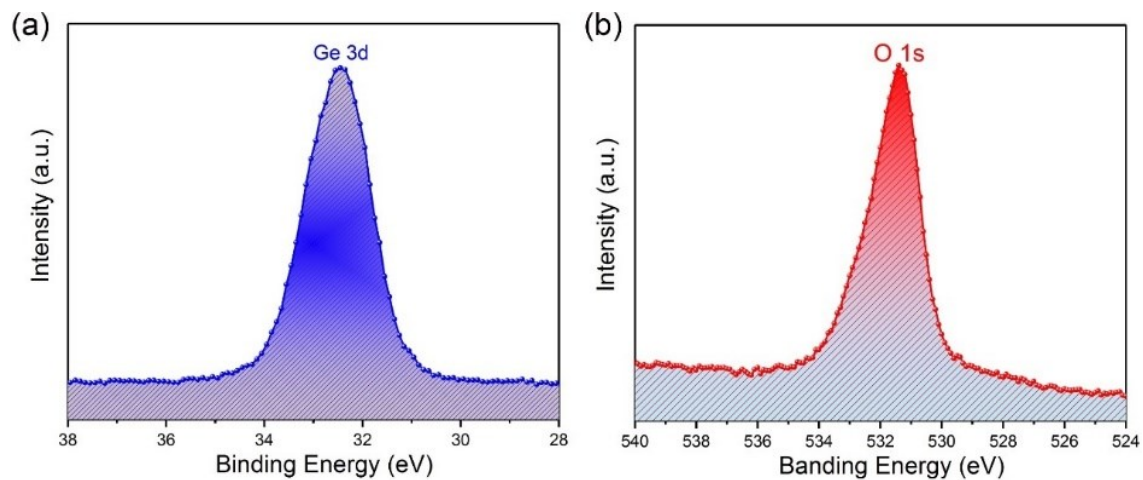


Figure S10. XPS spectra of Ge 3d (a) and O 1s (b) of rutile-type GeO₂.

14. UV-Vis diffuse reflectance spectra of rutile GeO₂

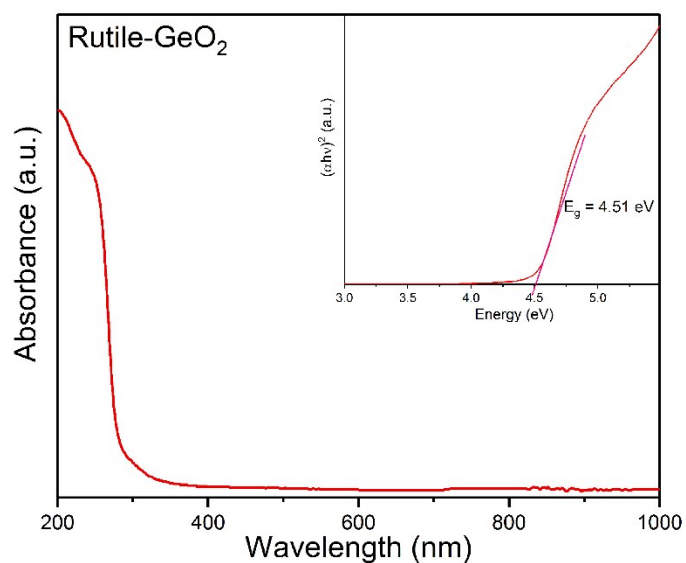


Figure S11. UV-Vis diffuse reflectance spectra of the rutile-type GeO₂. The inset shows the plot of $(\alpha h\nu)^2$ against the photon energy ($h\nu$).

15. Photocatalytic H₂ evolution rate for rutile TiO₂, GeO₂, and GeO₂ loaded various cocatalyst

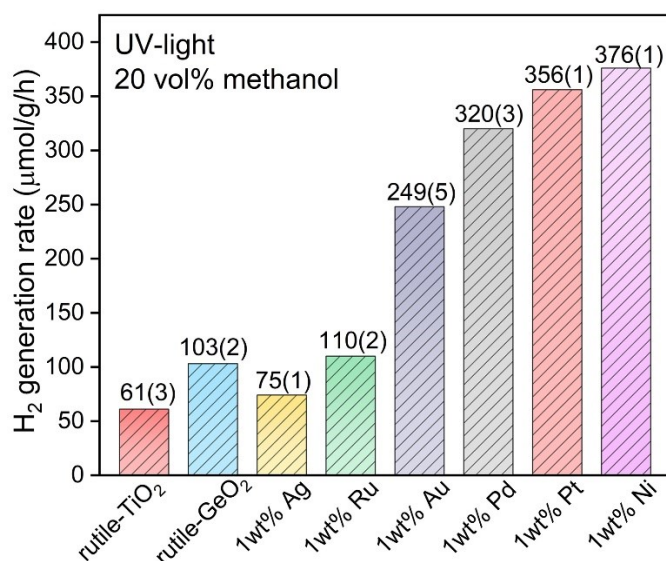


Figure S12. H₂ evolution rates for the rutile-type TiO₂ and GeO₂, as well as rutile-type GeO₂ loaded with various cocatalysts including Ag, Ru, Au, Pd, Pt, and Ni.

16. Repeating photocatalytic experiment for rutile GeO₂ in pure water system

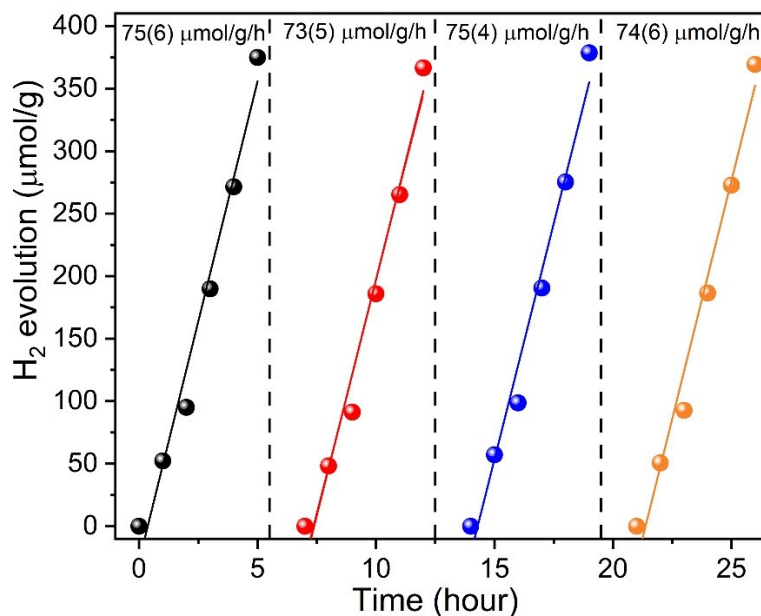


Figure S13. Time-dependence of H₂ evolution for rutile GeO₂ in pure water system. After each cycle, the system was evacuated.

17. Powder XRD for rutile GeO_2 before and after the photocatalytic reactions

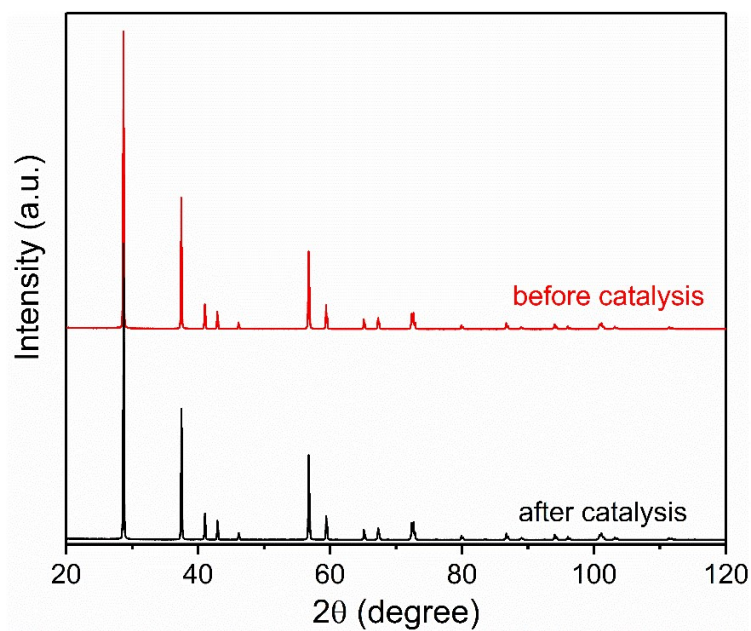


Figure S14. Powder XRD for rutile-type GeO_2 before and after the photocatalytic reactions.

18. Powder XRD for rutile GeO_2 and the melon- GeO_2 composite

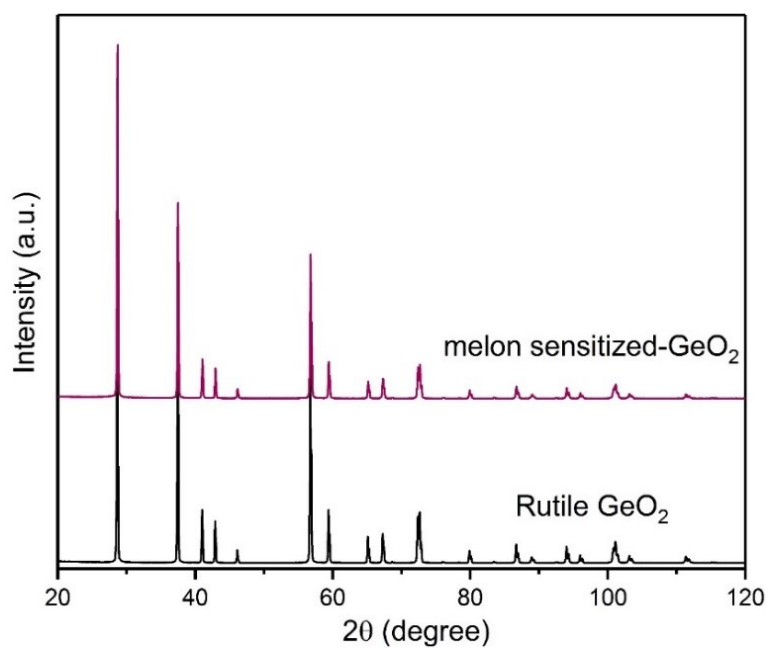


Figure S15. The comparison of XRD patterns of rutile GeO_2 and the melon- GeO_2

composite. It almost has no change with the single component GeO_2 after modifying melon. Most reports suggested that melon has a main broad peak around the 27-29 degree,¹² here it is not observed due to the small quantity and the low crystallinity compared to the GeO_2 .

19. High-resolution XPS spectra of the melon- GeO_2 composite

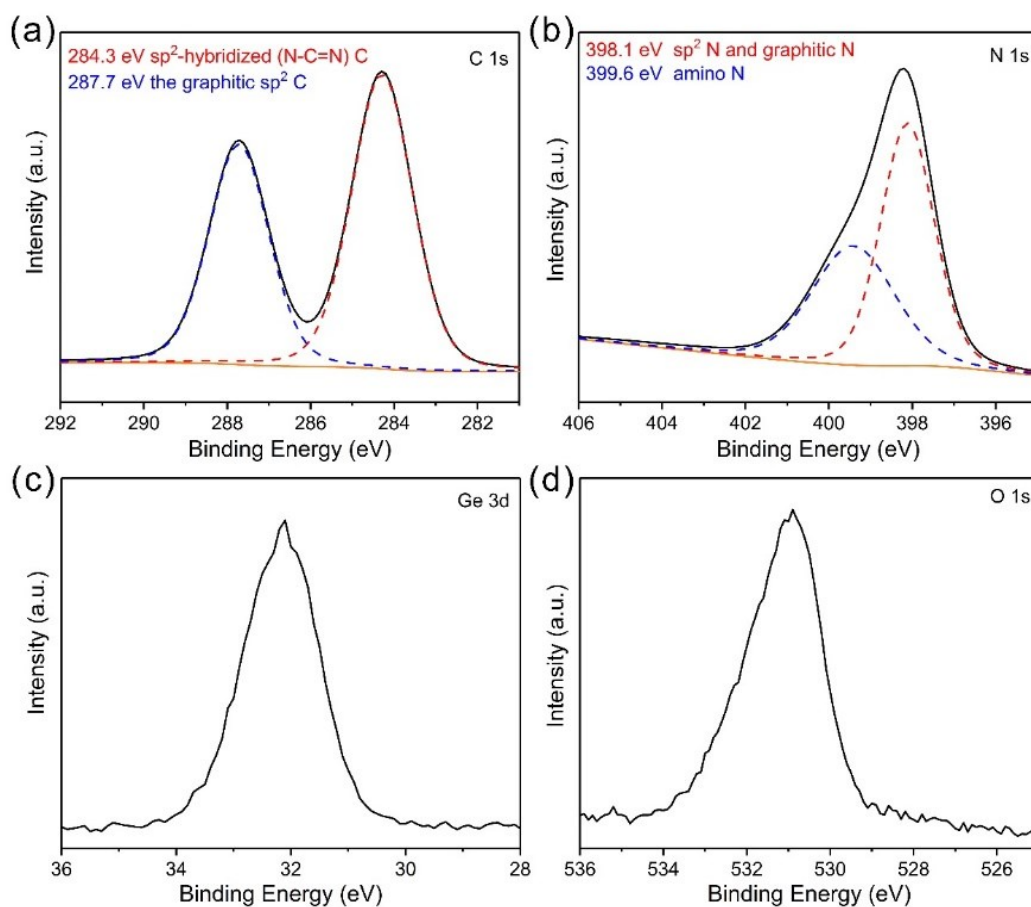


Figure S16. The high-resolution XPS spectra of (a) C 1s, (b) N 1s, (c) Ge 3d and (d) O 1s for the melon- GeO_2 composite photocatalyst. In light of the binding energies of C 1s and N 1s core electrons, two C 1s peaks at 284.3 eV and 287.7 eV originate from the sp^2 C-N=C hybridized coordination and the graphitic sp^2 C-C bonds of melon, respectively. Meanwhile, the broad peak of N 1s is attributed to the sp^2 hybridized N, graphitic N and amino N of melon.¹²

20. UV Raman spectra of the melon-GeO₂ composite

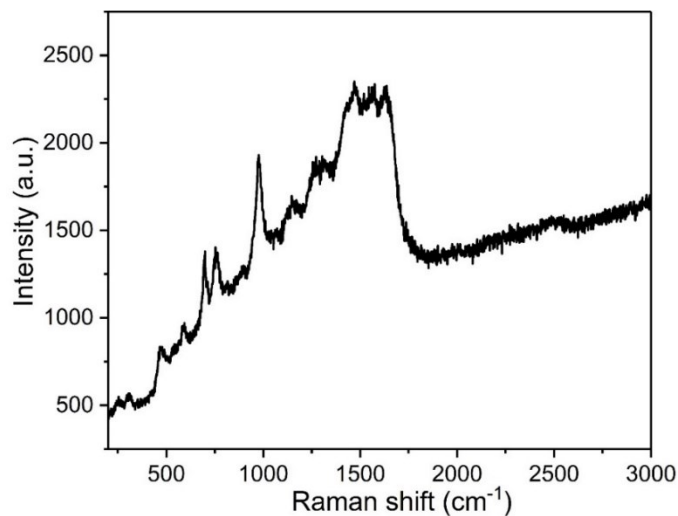


Figure S17. UV Raman spectra of the melon-GeO₂ composite. Raman spectrum was obtained under UV excitation (325 nm) to eliminate the effect of intense fluorescence. The sharp peak at 980 cm⁻¹ is due to the triazine units, which constitute the structure of melon polymer. A series of peaks at 1200-1700 cm⁻¹ were assigned to the fundamental C-N stretching vibrations.¹³

21. Typical thermogravimetric curve of the melon-GeO₂ composite

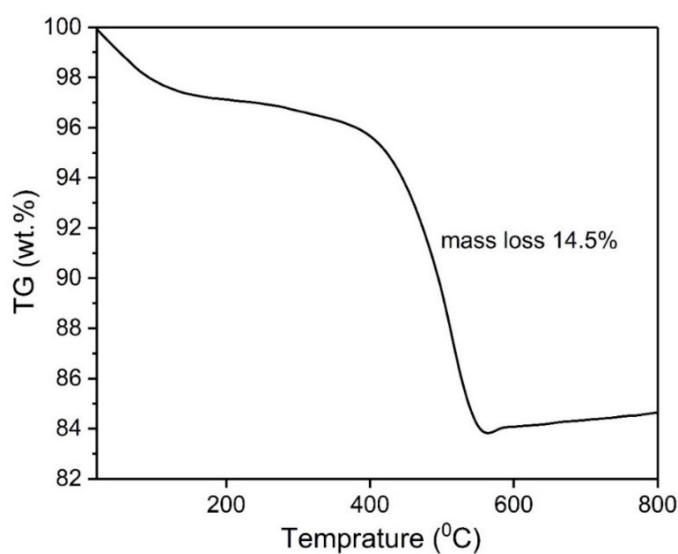


Figure S18. The typical thermogravimetric graph of the melon-GeO₂ composite in the temperature range from room temperature to 800 °C. Two mass losses at RT-150 °C

and 400-560 °C ranges were detected. The first 3 wt% mass loss is due to the loss of water molecule and the hydroxyl groups on the surface. The second 12 wt% mass loss was attributed to the decomposition of C-N structure framework of melon.¹⁴

22. UV-vis spectra of the melon-GeO₂ composite

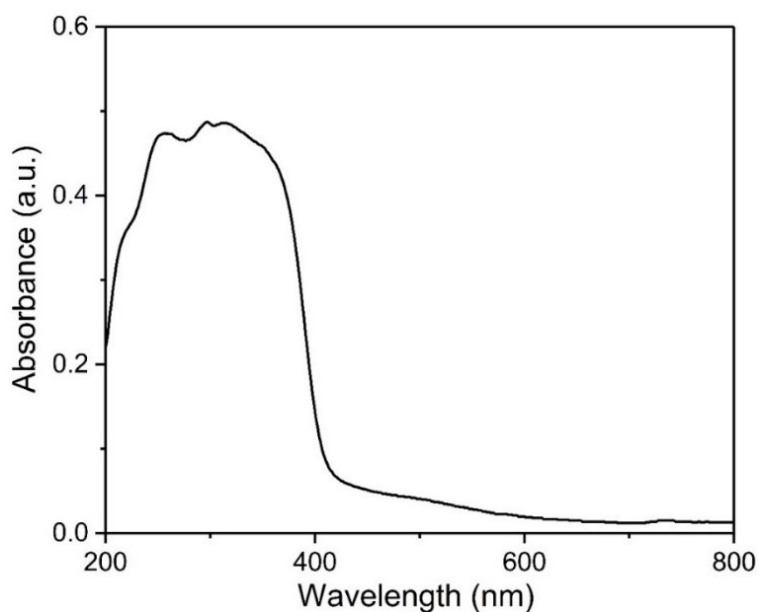


Figure S19. UV-Vis spectra of the melon-GeO₂ composite. As expected, the UV-Vis DRS spectrum confirms the visible light response, and the obvious red-shift of the absorption edge from 280 nm to 410 nm was detected.

23. Repeating photocatalytic experiment for the melon-GeO₂ composite

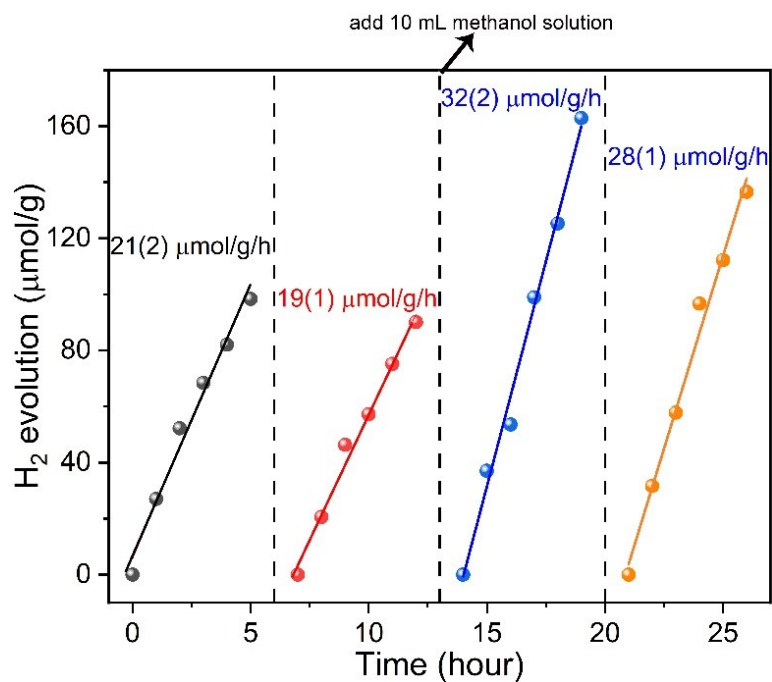


Figure S20. Time-dependence of H₂ evolution for the melon-GeO₂ composite photocatalyst in pure water (for first two cycles) and methanol aqueous solution (for the last two cycles). After each cycle, the system was evacuated.

24. Work functions for monolayer melon, GeO₂ (100) surface, and the melon-GeO₂ composite.

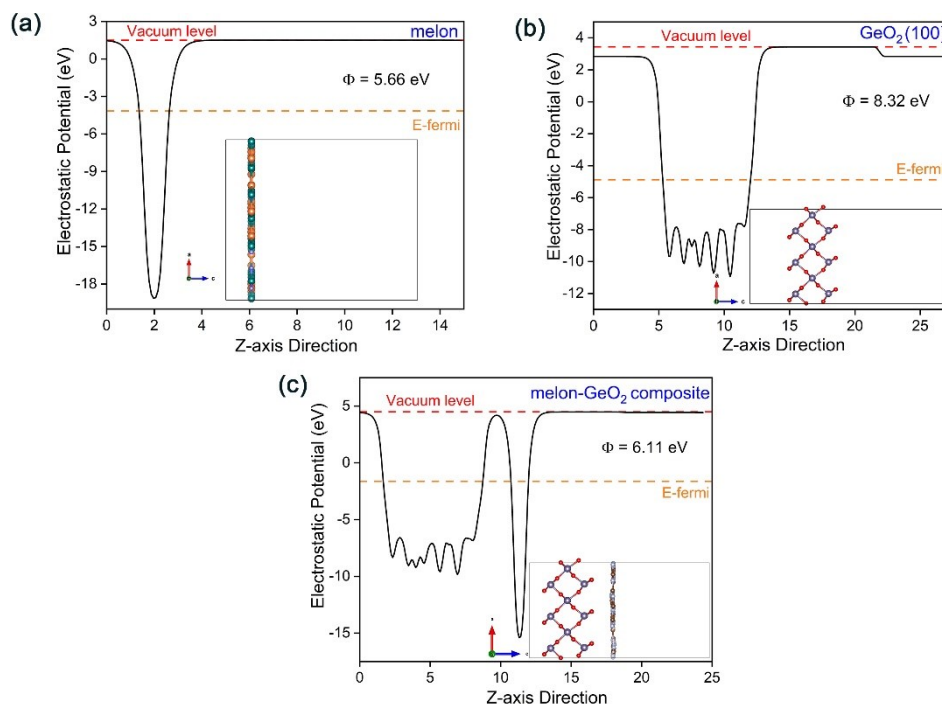


Figure S21. Calculated electrostatic potentials for (a) monolayer melon, (b) GeO₂ (100) surface, (c) melon-GeO₂ composite model.

25. The band alignment of GeO₂ and melon before contacting.

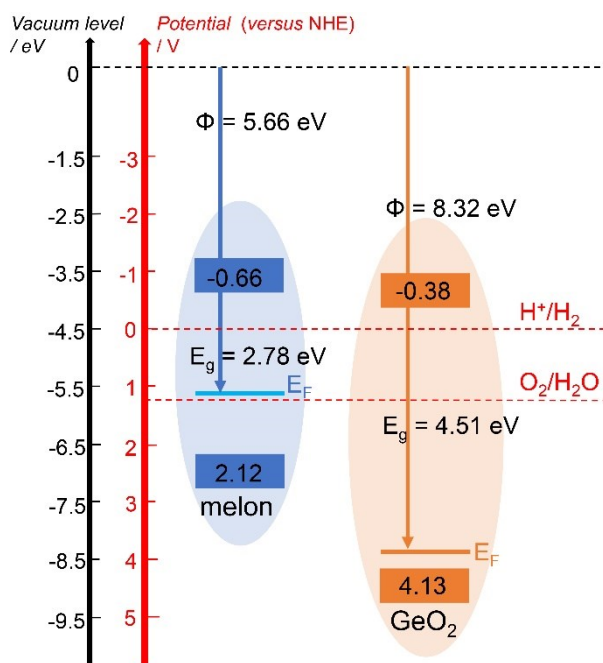


Figure S22. The positions of CB (LUMO) and VB (HOMO) for bulk rutile GeO₂ and melon. The LUMO and HOMO orbitals of melon locate at -0.66 eV and 2.12 eV versus

NHE, respectively.⁹ E_{CB} and E_{VB} of GeO_2 are -0.38 eV and 4.13 eV, respectively, according to the Mulliken electronegativity theory.¹⁵

26. Table of calculated effective masses of charges for rutile TiO_2 and GeO_2

Table S1. Calculated effective masses of carriers along the [110] and [001] directions for rutile TiO_2 and GeO_2

		Direction	m_e^*/m_0	m_h^*/m_0	m_h^*/m_e^*
TiO₂	G→M		1.502	4.664	3.105
	[110]				
	G→Z [001]		0.561	6.868	12.242
GeO₂	G→M		0.219	0.966	4.411
	[110]				
	G→Z [001]		0.192	1.597	8.318

27. Table of calculated effective masses of charges for rutile SnO_2

Table S2. Calculated effective masses of carriers along the [100], [110] and [001] directions for rutile SnO_2

		Effective mass	
		m_e^*/m_0	m_h^*/m_0
Ref.⁷		0.168 (G→X)	1.309 (G→X)
		0.157 (G→Z)	1.864 (G→Z)
Our result		0.192 (G→X)	1.298 (G→X)
		0.190 (G→M)	1.422 (G→M)
		0.173 (G→Z)	1.809 (G→Z)

28. Table of calculated effective masses of charges for α -quartz GeO_2

Table S3. Calculated effective masses of carriers along the [001] and [100] directions for α -quartz GeO₂

Direction	m_e^*/m_0	m_h^*/m_0	m_h^*/m_e^*
G→A [001]	0.368	2.014	5.473
G→M [100]	0.412	-----	

29. The calculation of the potentials of CB and VB edges for rutile GeO₂

The potentials of CB and VB edges of rutile GeO₂ were calculated by the following equations:¹⁵

$$E_{VB} = \chi - E_e + \frac{1}{2}E_g$$

$$E_{CB} = E_{VB} - E_g$$

where χ is the Mulliken electronegativity of GeO₂, which is calculated about 6.38 eV, and E_e is the energy of free electron on the hydrogen scale (4.5 eV). E_g is the measured band gap by UV-vis DRS. Finally, the calculated values of E_{CB} and E_{VB} were -0.38 eV and 4.13 eV, respectively.

30. References

- (1) *TOPAS, V4.1-beta*, Bruker AXS, Karlsruhe, Germany, 2004.
- (2) Yang, J.; Jiang, P.-F.; Yue, M.-F.; Yang, D.-F.; Cong, R.-H.; Gao, W.-L.; Yang, T. Bi₂Ga₄O₉: An Undoped Single-Phase Photocatalyst for Overall Water Splitting under Visible Light. *J. Catal.* **2017**, *345*, 236-244.
- (3) (a) Kresse, G.; Furthmuller, J. Efficient Iterative Schemes for *ab initio* Total-Energy Calculations using a Plane-Wave Basis Set. *Phys. Rev. B* **1996**, *54*, 11169-11186;
 (b) Kresse, G.; Furthmuller, J. Efficiency of Ab-initio Total Energy Calculations for Metals and Semiconductors using a Plane-Wave Basis Set. *Comp. Mater. Sci.* **1996**, *6*, 15-50.

- (4) Blochl, P. E. Projector Augmented-Wave Method. *Phys. Rev. B* **1994**, *50*, 17953-17979.
- (5) Perdew, J. P.; Burke, K.; Ernzerhof, M. Generalized Gradient Approximation Made Simple. *Phys. Rev. Lett.* **1996**, *77*, 3865-3868.
- (6) Heyd, J.; Scuseria, G. E.; Ernzerhof, M. Hybrid Functionals Based on a Screened Coulomb Potential. *J. Chem. Phys.* **2003**, *118*, 8207-8215.
- (7) Li, Y.-Y.; Yang, Q.-M.; Wang, Z.-M.; Wang, G.-Y.; Zhang, B.; Zhang, Q.; Yang, D.-F. Rapid Fabrication of SnO₂ Nanoparticle Photocatalyst: Computational Understanding and Photocatalytic Degradation of Organic Dye. *Inorg. Chem. Front.* **2018**, *5*, 11.
- (8) Maintz, S.; Deringer, V. L.; Tchougreeff, A. L.; Dronskowski, R. LOBSTER: A Tool to Extract Chemical Bonding from Plane-Wave Based DFT. *J. Comput. Chem.* **2016**, *37*, 1030-1035.
- (9) Niu, P.; Yin, L.-C.; Yang, Y. Q.; Liu, G.; Cheng, H.-M. Increasing the Visible Light Absorption of Graphitic Carbon Nitride (Melon) Photocatalysts by Homogeneous Self-Modification with Nitrogen Vacancies. *Adv. Mater.*, **2014**, *26*, 8046-8052.
- (10) Sorantin, P. I.; Schwarz, K. Chemical Bonding in Rutile-Type Compounds. *Inorg. Chem.* **1992**, *31*, 567-576.
- (11) Mizoguchi, H.; Woodward, P. M. Electronic Structure Studies of Main Group Oxides Possessing Edge-Sharing Octahedra: Implications for the Design of Transparent Conducting Oxides. *Chem. Mater.* **2004**, *16*, 5233-5248.
- (12) Lau, V. M. H.; Moudrakovski, I.; Botari, T.; Weinberger, S.; Mesch, M. B.; Duppel, V.; Senker, J.; Blum, V.; Lotsch, B. V. Rational Design of Carbon Nitride Photocatalysts by Identification of Cyanamide Defects as Catalytically Relevant Sites. *Nat. Commun.* **2016**, *7*, 12165.
- (13) McMillan, P. F.; Lees, V.; Quirico, E.; Montagnac, G.; Sella, A.; Reynard, B.; Simon, P.; Bailey, E.; Deifallah, M.; Cora, F. Graphitic Carbon Nitride C₆N₉H₃·HCl: Characterisation by UV and near-IR FT Raman Spectroscopy. *J. Solid State Chem.* **2009**, *182*, 2670-2677.

- (14) Ang, T. P. Sol-Gel Synthesis of a Novel Melon-SiO₂ Nanocomposite with Photocatalytic Activity. *Catal. Commun.* **2009**, *10*, 1920-1924.
- (15) Lin, X. P.; Xing, J.-C.; Wang, W.-D.; Shan, Z.-C.; Xu, F.-F.; Huang, F.-Q. Photocatalytic Activities of Heterojunction Semiconductors Bi₂O₃/BaTiO₃: A strategy for the Design of Efficient Combined Photocatalysts. *J. Phys. Chem. C* **2007**, *111*, 18288-18293.